PHYSICAL REVIEW FLUIDS **7**, 114301 (2022)

# Evaporation and clustering of ammonia droplets in a hot environment

Lorenzo Angelilli,[*] Francisco E. Hernández Pérez, and Hong G. Im
*Physical Science and Engineering, Clean Combustion Research Center, King Abdullah University of Science and Technology, Thuwal 23955, Saudi Arabia*

Pietro Paolo Ciottoli and Mauro Valorani
*Department of Aerospace and Mechanical Engineering, Sapienza - University of Rome, Via Eudossiana 18, 00184 Rome, Italy*

(Received 12 June 2022; accepted 20 September 2022; published 9 November 2022)

Recent developments in the transition to zero-carbon fuels show that ammonia is a valid candidate for combustion. However, liquid ammonia combustion is difficult to stabilize due to a large latent heat of evaporation, which generates a strong cooling effect that adversely affects the flame stabilization and combustion efficiency. In addition, the slow burning rate of ammonia enhances the undesired production of $NO_x$ and $N_2O$. To increase the flame speed, ammonia must be blended with a gaseous fuel having a high burning rate. In this context, a deeper understanding of the droplet dynamics is required to optimize the combustor design. To provide reliable physical insights into diluted ammonia sprays blended with gaseous methane, direct numerical simulations are employed. Three numerical experiments were performed with cold, standard, and hot ambient in nonreactive conditions. The droplet radius and velocity distribution, as well as the mass and heat coupling source terms are compared to study the effects on the evaporation. Since the cooling effect is stronger than the heat convection between the droplet and the environment in each case, ammonia droplets do not experience boiling. On the other hand, the entrainment of dry air into the ammonia-methane mixture moves the saturation level beyond 100% and droplets condense. The aforementioned phenomena are found to strongly affect the droplet evolution. Finally, a three-dimensional Voronoi analysis is performed to characterize the dispersive or clustering behavior of droplets by means of the definition of a clustering index.

DOI: 10.1103/PhysRevFluids.7.114301

## I. INTRODUCTION

Decarbonization of fuels is one of the key objectives of the combustion community to reduce the emission of pollutants and greenhouse gases [1]. Ammonia ($NH_3$) is a valid candidate to substitute traditional fossil fuels because of the absence of carbon in its molecular composition, as well as its low boiling temperature at atmospheric pressure ($T_{\text{boil}} = 239\,\text{K}$), which allows its storage in liquid phase at a relatively low pressure (approximately 10 atm) while guaranteeing a rapid vaporization

---

[*] lorenzo.angelilli@kaust.edu.sa

that is mainly driven by flash boiling [2]. On the other hand, due to the presence of nitrogen in the molecular composition of ammonia, the combustor operative conditions must be carefully selected, in terms of pressure and temperature, to minimize the generation of $NO_x$ and $N_2O$ [3,4]. Moreover, the ammonia burning rate is significantly lower, compared to hydrogen or hydrocarbon fuels, thus it may be necessary to blend ammonia with another gaseous fuel such as hydrogen or methane to stabilize the flame inside the burner [5].

Combustion of ammonia that is directly injected in gaseous phase has extensively been studied (see, e.g., recent reviews of Refs. [5,6]), yet the unique characteristics of polydispersed ammonia sprays have received scarce attention, while the subject has attracted growing interest for direct liquid ammonia injection into the combustor in order to achieve higher efficiencies. In this regard, Verkamp *et al.* [7] proposed several unsuccessful solutions to stabilize liquid ammonia flames by changing the inlet conditions of air such as velocity and temperature, observing that the flame was immediately blown off after turning off the igniter. Recently, Okafor *et al.* [8] proposed a swirl burner, obtaining stable combustion by the injection of hot air. An intense recirculation zone was generated in the combustor, which contributed to stabilizing the flame. However, the low burning rate of the $NH_3$-air flame promoted significant emissions of $N_2O$ and $NO_x$. To improve the stability of the flame and mitigate emissions, they opted to incorporate a coaxial pipe injecting methane into the burner. The blending of ammonia with a fuel having a higher burning rate supported the recombination of atomic nitrogen into the molecular one, reducing dramatically the pollutants at the expense of a tolerable amount of $CO_2$.

Although considerable advances have been made towards liquid ammonia combustion recently, most research efforts have focused on finding a solution to practical issues such as the flame stabilization or the control of pollutant emissions. However, there is a lack of understanding of fundamental aspects of the spray formation and evolution, which can be affected by flash boiling and a large latent heat of vaporization. Detailed understanding of the unique characteristics of the ammonia evaporating sprays is essential in designing new and retrofitted combustion systems using ammonia as the main fuel.

In this context, this work aims at providing a comprehensive analysis of the effects of the surrounding gas temperature on the evaporation and dispersion through point-particle direct numerical simulation (DNS) in nonreactive conditions. While the recent advances in the volume-of-fluid (VoF) approaches are able to describe the evaporation of the liquid phase [9] at much higher fidelity, a full VoF simulation of highly turbulent spray jet is not feasible with the modern computational resources. Subsequently, the authors preferred to adopt the canonical Lagrangian-Eulerian approach for the spray description. The adoption of point-particle DNS to investigate the spray dynamics allows us to understand phenomena occurring at scales that are not observable by the traditional experimental facilities, such as the role of mass and heat exchange and the dispersion patterns [10–12]. Such phenomena become crucial to design liquid ammonia combustors, where the large latent heat is responsible for the cooling effect on the combustion [8].

The configuration adopted in this study is based on the one employed by Chen *et al.* [13], and the gaseous composition and liquid droplets initial conditions are selected to be similar to those of the swirled ammonia spray burner configuration of Okafor *et al.* [8]. Three simulations with common inflow conditions and varying ambient temperature are performed: (a) with a cold environment temperature $T_a = 220\,\mathrm{K}$, for which the evaporation is mainly driven by diffusion; (b) at the standard condition ($T_a = 300\,\mathrm{K}$), to examine the evolution of ammonia droplets under a surrounding temperature that is slightly higher than the boiling temperature at atmospheric pressure; and (c) with $T_a = 600\,\mathrm{K}$, to investigate the effects of a considerably hot environment.

By means of an extensive analysis of the droplet statistics of the main scalars characterizing the droplets, the effects of environment temperature on evaporation and dispersion are described and quantified. In particular, the evaporation characteristics are examined in terms of the evolution of the droplet radius, mass and heat transfer source terms, and droplet velocity, while the dispersion is examined through the droplet distribution and a Voronoi [14] analysis.

The remainder of this paper is structured as follows. Section II reviews the theoretical framework describing evaporating spray dynamics in DNS contexts. Section III describes the numerical setup for the test cases that are considered. Section IV describes and discusses the peculiar spray characteristics of ammonia evaporation and dispersion. Finally, Sec. V summarizes and concludes the paper.

## II. NUMERICAL MODEL

An Eulerian-Lagrangian approach is employed to describe the two-phase flow. The fully compressible conservation equations for the transport of the mass, momentum, and energy are solved. The ideal gas equation of state was employed since the reduced temperature and pressure are $T_{red} = 0.52$ and pressure $p_{red} = 0.009$ for the lowest temperature corresponding to a compressibility factor of $z = 0.997$. The Eulerian Navier-Stokes equations involve an additional source term related to the two-way coupling [15]. The equations are summarized as:

$$\frac{\partial}{\partial t}(\rho Y_\alpha) + \nabla \cdot (\rho \mathbf{U} Y_\alpha) + \nabla \cdot \mathbf{J}_\alpha = \dot{S}_\alpha \quad \text{for} \quad \alpha = 1, \ldots, N, \tag{1}$$

$$\frac{\partial}{\partial t}(\rho \mathbf{U}) + \nabla \cdot (\rho \mathbf{U}\mathbf{U}) = \nabla p + \nabla \cdot \bar{\tau} + \dot{\mathbf{S}}_{ev} + \dot{\mathbf{S}}_f, \tag{2}$$

and

$$\frac{\partial}{\partial t}(\rho E) + \nabla \cdot (\rho H \mathbf{U}) = \nabla \cdot \mathbf{J}_h + \dot{S}_{ht} + \dot{S}_{mt}, \tag{3}$$

where $\rho$ is the carrier mixture density, $Y_\alpha$ is species $\alpha$ mass fraction, $\mathbf{U}$ is gas velocity vector,

$$E = e + \tfrac{1}{2}\mathbf{U} \cdot \mathbf{U}$$

is the total internal energy, and

$$H = h + \tfrac{1}{2}\mathbf{U} \cdot \mathbf{U}$$

is the total enthalpy.

The species equation includes the molecular diffusive flux, approximated by Fick's law,

$$\mathbf{J}_\alpha = -\rho D_\alpha \nabla Y_\alpha, \tag{4}$$

where $D_\alpha$ is the mass diffusion coefficient into the most abundant species.

Since $\sum_\alpha Y_\alpha = 1$, and $\sum_\alpha \mathbf{J}_\alpha = \mathbf{0}$, summing Eq. (1) over all species $\alpha$ yields the total mass conservation, where $N - 1$ species equations are solved and the $N$th species is obtained from $\sum_\alpha Y_\alpha = 1$.

The momentum equation (2) includes the viscous stress tensor,

$$\tau_{ij} = \mu \left( \frac{\partial U_i}{\partial x_j} + \frac{\partial U_j}{\partial x_i} - \delta_{ij} \frac{2}{3} \frac{\partial U_k}{\partial x_k} \right), \tag{5}$$

where $\mu$ is the dynamic viscosity (a function of temperature), and $\delta_{ij}$ is the Kronecker delta function.

The energy equation (3) includes the enthalpy diffusive flux,

$$\mathbf{J}_h = \lambda \nabla T - \sum_{\alpha=1}^{N} h_\alpha \mathbf{J}_\alpha + \bar{\tau}\mathbf{U}, \tag{6}$$

where $T$ is the temperature, $\lambda$ is the thermal conductivity, and $h_\alpha$ is the specific enthalpy for species $\alpha$.

Equations (1)–(3) also include additional source terms accounting for the interactions with Lagrangian particles. The present study represents each droplet as a single Lagrangian point with designated mass, temperature, and composition. This approximation applies to a single droplet evolution even in the DNS context, provided that the droplet radius is sufficiently smaller than the Kolmogorov length, and thus smaller than the computational cell [16–18]. The source terms for $n_d$ droplets in the computational domain are expressed as

$$\dot{S}_{m_\alpha} = \sum_{k=1}^{n_d} \dot{m}_d^{k_\alpha}(t)\hat{g}\big(\left|x - X_d^k(t)\right|\big), \tag{7}$$

$$\dot{\mathbf{S}}_{ev} = \sum_{k=1}^{n_d}\sum_{\alpha=1}^{N} \dot{m}_d^{k_\alpha}(t)\mathbf{U}_d^k(t)\hat{g}\big(\left|x - X_d^k(t)\right|\big), \tag{8}$$

$$\dot{\mathbf{S}}_{f} = \sum_{k=1}^{n_d} \mathbf{f}_d^{k}(t)\hat{g}\big(\left|x - X_d^k(t)\right|\big), \tag{9}$$

$$\dot{S}_{mt} = \sum_{k=1}^{n_d}\sum_{\alpha=1}^{N} \dot{m}_d^{k_\alpha}(t)h_d^{k_\alpha}(t)\hat{g}\big(\left|x - X_d^k(t)\right|\big), \tag{10}$$

and

$$\dot{S}_{ht} = \sum_{k=1}^{n_d}\sum_{\alpha=1}^{N} \dot{h}_d^{k_\alpha}(t)m_d^{k_\alpha}(t)\hat{g}\big(\left|x - X_d^k(t)\right|\big), \tag{11}$$

where $m_d^{k_\alpha}$ and $h_d^{k_\alpha}$ are the mass and enthalpy of $\alpha$th species inside the $k$th droplet, and subscripts denote species $\alpha$ mass addition by species evaporation ($m_\alpha$), momentum by evaporation ($ev$), momentum by external forces ($f$), and energy by mass ($mt$) and heat ($ht$) transfer. All source terms are computed as a sum over $k$ droplets, and the kernel function $\hat{g}(x)$ indicates the domain of the source term's influence [15]. In the DNS, the kernel function is usually assumed to be the Dirac $\delta$ function since the exact droplet position is resolved [19].

In the following, superscript $k$ and subscript $\alpha$ are omitted in the notation for brevity. A Lagrangian droplet is characterized by its position in time, which is governed by Newton's law,

$$\frac{d(m_d\mathbf{V}_d)}{dt} = \mathbf{f}_d, \tag{12}$$

with the corresponding droplet mass and enthalpy expressed as:

$$\frac{dm_d}{dt} = \dot{m}_d, \tag{13}$$

$$\frac{dh_d}{dt} = \dot{h}_d, \tag{14}$$

where $\dot{m}_d$ is the mass transfer rate, including evaporation ($\dot{m}_d > 0$) and condensation ($\dot{m}_d < 0$); and $\dot{h}_d$ is the enthalpy transfer rate due to heat conduction and diffusion effects. The trajectory of the single droplet is then given by the equation:

$$\frac{d^2\mathbf{X}^D}{dt^2} = \frac{d\mathbf{V}_d}{dt} = \frac{\mathbf{f}_d}{m_d} - \frac{1}{m_d}\frac{dm_d}{dt}\mathbf{V}_d = \frac{\mathbf{f}_d}{m_d} + \frac{\dot{m}_d}{m_d}\mathbf{V}_d. \tag{15}$$

The constitutive models for the source terms in Eqs. (12)–(14) are described next. The momentum exchange is modeled as

$$\mathbf{f}_d \approx \frac{m_d}{\tau^D}C_D(\mathrm{Re}_d)\Delta\mathbf{U}, \tag{16}$$

where $\mathrm{Re}_d = 2r_d|\Delta\mathbf{U}|/\nu_g$ is the droplet Reynolds number, $r_d$ is the droplet radius assuming all droplets are spherical, $\Delta\mathbf{U}$ is the droplet relative velocity, $\nu_g$ is the kinematic viscosity of the gaseous phase. The aerodynamic relaxation time $\tau^D$ is defined as

$$\frac{1}{\tau^D} = \frac{18\mu_g}{(2r_d)^2\rho_l}, \tag{17}$$

and the drag coefficient is expressed using the Schiller-Neumann correlation [19],

$$C_D(\mathrm{Re}_d) = \begin{cases} 1 + \frac{3}{20}\mathrm{Re}_d^{0.687} & \text{if} \quad \mathrm{Re}_d \leqslant 1000 \\ \frac{11}{600}\mathrm{Re}_d & \text{if} \quad \mathrm{Re}_d > 1000. \end{cases} \tag{18}$$

Mass exchange is driven by the classical rapid mixing model formulated by Spalding [20] and Godsave [21],

$$\dot{m}_d(t) = -\frac{\mathrm{Sh}_d}{3\mathrm{Sc}_g}\left(\frac{m_d}{\tau^D}\right)\ln\left(B_M + 1\right), \tag{19}$$

where

$$B_M = \frac{Y_s - Y_\infty}{1 - Y_s} \tag{20}$$

is the Spalding coefficient, and $Y_s$ and $Y_\infty$ are mass fractions for the evaporating species at the droplet surface and far field, respectively.

Following Abramzon and Sirignano [18], $Y_\infty$ and $T_\infty$ for each droplet are substituted by the values in the computational cell containing the droplet. A droplet is assumed isothermal with temperature $T_d$. Liquid-vapor equilibrium is assumed at the droplet surface, hence evaporated liquid at the droplet surface is the saturated vapor mass fraction at temperature $T_d$, evaluated by interpolation of the NIST database.

The corresponding mass fraction is expressed as

$$Y_s = \frac{X_{\mathrm{sat}}W_\alpha}{X_{\mathrm{sat}}W_\alpha + (1 - X_{\mathrm{sat}})W_{n\alpha}}, \tag{21}$$

where $W_\alpha$ and $W_{n\alpha}$ are molar masses for the $\alpha$th evaporating species and carrier gas mixture excluding the evaporating species, respectively, and subscript $g$ denotes carrier gas properties in the droplet surroundings. Yuen and Chen [22] proposed a linear mixing model to estimate temperature $[T_g = T_d + (T_\infty - T_d)/3]$ and composition $[Y_g = Y_s + (Y_\infty - Y_s)/3]$, evaluating gas properties at the corresponding $T_g$ and $Y_g$.

The turbulent convective effects are accounted for by the Schmidt number $[\mathrm{Sc}_g = \mu_g/(\rho_g D)]$, and Sherwood number ($\mathrm{Sh} = 2K_c r_d/D$, with $K_c$ being the convective mass exchange coefficient), evaluated by the Frossling correlation [19] as

$$\mathrm{Sh}_D = 2 + 0.552{\mathrm{Re}_d}^{1/2}\mathrm{Sc}_g^{1/3}. \tag{22}$$

The enthalpy exchange rate is modeled by the infinite conductivity approach [19], with

$$\dot{h}_d = f_1\frac{\mathrm{Nu}_d}{3\mathrm{Pr}_g}C_{P,g}\frac{T_g - T_d}{\tau^D} - \frac{\dot{m}_d}{m_d}L_v, \tag{23}$$

where $\mathrm{Pr}_g = \mu_g C_{p,g}/\lambda_g$ is the Prandtl number based on the surrounding gas properties, and $C_{p,g}$ is the heat capacity at constant pressure. The droplet Nusselt number, $\mathrm{Nu}_d$, is estimated by the correlation

$$\mathrm{Nu}_d = 2 + 0.552{\mathrm{Re}_d}^{1/2}\mathrm{Pr}_g^{1/3}, \tag{24}$$

and the Stefan-flow correction factor $f_1$ is evaluated following Miller *et al.* [19]:

$$f_1 = \frac{\beta}{e^\beta - 1}, \tag{25}$$

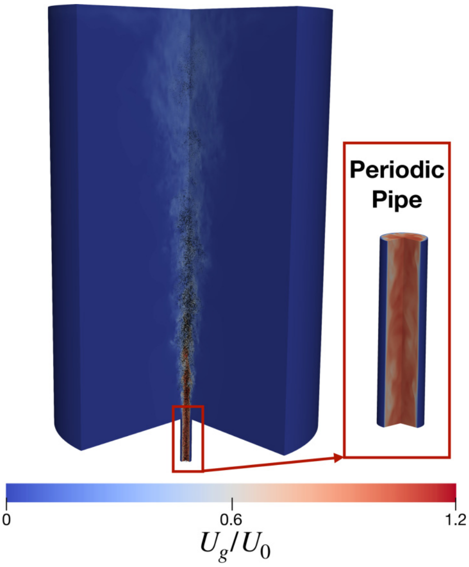

FIG. 1. Sector of the computational domain displaying the magnitude of the velocity field.

and

$$\beta = -\left(\frac{3\mathrm{Pr}_g\tau^D}{2}\right)\frac{\dot{m}_d}{m_d}.$$

## III. TEST CASE AND VALIDATION

The present campaign aims at examining the dynamics of liquid ammonia droplets dispersed in a gaseous jet of ammonia and methane. The key parameter is the environmental temperatures at atmospheric pressure. The test case was inspired by the experimental configuration by Chen *et al.* [13], where liquid acetone droplets are injected and dispersed in a gaseous mixture of acetone and air. The saturation conditions are enforced at the inflow in order to ensure thermal equilibrium and prevent the droplet evaporation inside the injector. This experimental configuration has been successfully modeled by researchers [10–12,23]. In the present study, the acetone droplets were substituted by pure ammonia droplets and the gaseous jet by a mixture of 45.2% ammonia and 54.8% methane by volume, corresponding to the saturation mass fraction of ammonia at atmospheric pressure. This composition of the gaseous phase and the initial condition of the liquid droplets follow the experimental study by Okafor *et al.* [8].

Figure 1 illustrates the entire cylindrical computational domain of the configuration under study. The radius of the cylinder is $10D$, its length is $40D$, and it is discretized by a staggered stretched mesh having 320 points on the radius and 720 on the height for a total of $64 \times 10^6$ cells. The lower base is represented by an adiabatic wall, whereas the upper outlet is treated by nonreflective boundary conditions. Convective boundary conditions were imposed at the lateral surface to allow the entrainment of air from outside the domain. The maximum ratio of the cell size ($\Delta$) to the Kolmogorov length scale ($\eta$) is $\Delta/\eta \approx 1.87$ in all the domain. The grid convergence is discussed in the Supplemental Material [24].

Three simulations were performed at a different temperature of the quiescent environment (air): (a) $T_a = 220\,\mathrm{K}$, (b) $T_a = 300\,\mathrm{K}$, and (c) $T_a = 600\,\mathrm{K}$.

Following the method by Dalla Barba and Picano [10,23], the inflow is generated by a three-dimensional fully turbulent periodic pipe of diameter $D = 0.01$ m with a bulk velocity at $U_0 = 8.1\,\mathrm{m/s}$, corresponding to a Reynolds number of 8640. To enforce the turbulence inside the pipe,

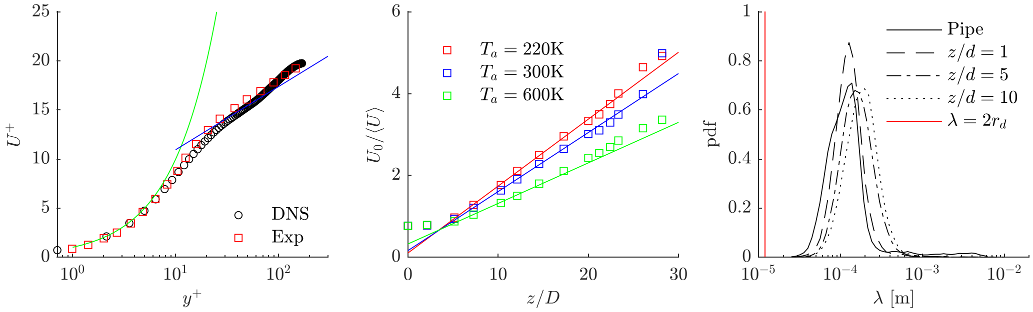

(a) (b) (c)

FIG. 2. (a) Universal log profile of the cylindrical pipe boundary layer ($U^+ = f(y^+)$). Black circles: reference DNS; red squares: experimental results of Eggels *et al.* [28]; green solid line: viscous sublayer profile $U^+ = y^+$; blue solid line: fitting of the log-law for the turbulent boundary layer $U^+ = k^{-1}\ln y^+ + B$, with $k = 0.43$ and $B = 4.8$. (b) Inverse of the average axial velocity for the three cases. The squares are the DNS data and the solid line is the fitting of linear trend described by $U_0/\langle U\rangle \approx 1/(2B)(z/R - z_0/R)$. The decaying constants are $B_{T_a=220K} = 3.05$, $B_{T_a=300K} = 3.45$, $B_{T_a=600K} = 5.05$, whereas the virtual origins are $z_{0,T_a=220K}/R = 0.61$, $z_{0,T_a=300K}/R = 1.11$, and $z_{0,T_a=600K}/R = 3.25$. (c) Probability density function of the interdroplet distances inside the pipe (black solid line) and at different stages from the nozzle exit (see legend). The red line represents the collisional threshold criterion $\lambda = 2r_d$.

the pipe length is taken as $L_{\text{pipe}} = 5\,D$ and the velocity boundary condition is obtained by sampling the instantaneous velocity field at $3\,D$ from the inlet. The no-slip adiabatic boundary condition is adopted at the pipe walls. To discretize the inflow, we used an axis-symmetric uniform mesh with 128 points along the radius and 450 points across the pipe length. This is considered a sufficient level of resolution since $\Delta/\eta \approx 0.34$, where $\eta = (\nu^3/\varepsilon)^{1/4}$ is the Kolomogorov length scale with $\varepsilon$ being the turbulent dissipation rate, and $\Delta = (\Delta_x\Delta_y\Delta_z)^{1/3}$ is the cell size. A total number of $55.4 \times 10^6$ ammonia droplets per second with initial radius $r_{d,0} = 6\,\mu\text{m}$ were injected into the domain by randomly placing them at the pipe inlet. The initial velocity of the droplets was $V_{d,0} = 8.1\,\text{m/s}$ to allow the droplets to be immediately adapted to the turbulent flow in the pipe. The liquid-vapor thermal equilibrium was ensured by the temperature of droplets and gas ($T_{g,d} = 220$ K) being below the saturation temperature at atmospheric pressure ($T_{\text{sat}} = 239$ K). For the point-droplet approximation to be valid everywhere, the droplet diameter must be smaller than the Kolmogorov length scale and the cell size and the gas phase velocity must be accurately interpolated at the droplet position [25,26]. In this work, the largest droplet diameter and the smallest mesh resolution are found in the inflow pipe, for which $\Delta/(2r_d) \approx 3.26 > 1$, confirming the validity of the approximation. In addition, a second-order polynomial interpolation is employed to reconstruct the velocity at the droplet position. Furthermore, from an *a posteriori* analysis, the average Weber number based on the gas density [$We_g = (2\rho_g|\Delta\mathbf{U}|^2 r_d)/\sigma$, with $\sigma$ being the surface tension and $\Delta\mathbf{U}$ the relative velocity], was approximately 0.03. According to the definitions of critical Weber number ($We_c$) available in the literature [27], $\overline{We_g} \ll We_c$, and thus the breakup model was not considered in this study.

Figure 2 shows some statistics to prove the fidelity of the simulated inflow pipe. In particular, Fig. 2(a) shows the profile $U^+ = f(y^+)$ [where $U^+ = \langle U\rangle/u_\tau$, $y^+ = (yu_\tau)/\nu$ with $u_\tau = (\tau_w/\rho)^{1/2}$ and $\tau_w = \rho\nu\frac{d\langle U\rangle}{dy}|_{y=0}$] of the pipe (black circles) compared against the experimental results of Eggels *et al.* [28] (red squares). The point-particle DNS results capture the experimental data very well, for both the linear profile of the viscous sublayer $U^+ = y^+$ (red continuous line) and the log profile ($U^+ = k^{-1}\ln y^+ + B$, with $k = 0.43$ and $B = 4.8$) (blue solid line). The friction Reynolds number is estimated as $\text{Re}_\tau = u_\tau R/\nu \approx 170$.

Figure 2(b) provides the inverse of the normalized averaged axial velocity along the centerline as a function of the distance from the nozzle exit. In the far field, the following relation holds:

$$\frac{U_b}{\langle U \rangle} = \frac{1}{2B}\left(\frac{z}{R} - \frac{z_0}{R}\right), \tag{26}$$

where $B$ is an empirical and nonuniversal constant, and $z_0$ is the virtual origin of the jet, representing the location of an effective point source of momentum originating the jet in the far field. By a straight line fit for $z/D > 15$, the values of $B$ and $z_0$ are close to the ones generated by [29,30].

The liquid volume fraction prescribed at the pipe inlet is $\phi = 8 \times 10^{-5}$. For such a low value of the volume fraction, the collisional probability is sufficiently low to neglect collisions and coalescence of droplets, though droplet clusters and turbophoresis occurring inside the pipe may increase the chance of such events [31]. Qian *et al.* [32] identified two parameters to describe collision and coalescence events: the Weber number based on liquid density $[We_l = (2\rho_l|\Delta\mathbf{U}|^2 r_d)/\sigma]$ and the collisional parameter $\chi = \lambda/(2r_d)$, where $\lambda$ is the interdroplet distance. In particular, if $\chi > 1$, collisions are not expected to occur. Figure 2(c) shows the probability density function of the interdroplet distance $\lambda$ inside the pipe and at different stages far from the nozzle exit computed *a posteriori*. Since the probability of $\lambda < r_{d,0}$ is considerably less than 1%, the effects of collisions are negligible.

The simulations were carried out using the OPENFOAM framework [33], version 7. Specifically, a modified SPRAYFOAM solver that includes condensation was utilized. A second-order centered scheme was adopted for the spatial discretization and a second-order backward Euler method was employed for the time integration of the governing equations. The Lagrangian equations were integrated with a fourth-order Runge-Kutta method. Numerical instabilities may occur when the equations are integrated for small droplets [10]. For this reason, we set a threshold of $r_{th} = 0.6\,\mu\text{m}$, corresponding to the 99.6% of mass evaporated, under which droplets are removed from the computational domain, ensuring the global conservation laws by transferring all the mass, momentum, and enthalpy to the gaseous phase.

The campaign was performed on the Shaheen II supercomputer at King Abdullah University of Science and Technology (KAUST). Shaheen has 6174 dual-socket compute nodes based on 16-core Intel Haswell processors running at 2.3 GHz. Each node has 128 GB of DDR4 memory running at 2300 MHz. To perform each simulation, we employed 4096 cores distributed over 128 computational nodes for a total amount of about $10^6$ core hours, corresponding to a bulk time of nearly ten days.

## IV. RESULTS AND DISCUSSION

This section presents the key aspects of the point-particle DNS campaign through the observation of (i) instantaneous gaseous fields, (ii) probability density function of Lagrangian quantities, and (iii) Eulerian averages of Lagrangian scalars. In particular, (iii) were performed over a regular squared grid of $\ell/R = 0.2$, where $\ell$ is the length of the cell size [10]. We also tested a lower resolution of $\ell/R = 0.5$, and found that some details were not captured in the clustering index analysis, while a higher resolution of $\ell/R = 0.1$ did not lead to any noticeable difference.

Figure 3 shows the temperature field of the different cases together with the droplet distribution represented by the black dots for the first 15 nozzle diameters downstream the nozzle exit. In case (a), corresponding to $T_a = 220\,\text{K}$, the temperature of the inflow is the same as the temperature of the environment. The high mass diffusivity combined with a large latent heat of evaporation is responsible for a fast temperature drop in the jet region, by around 15 K, from the initial temperature in the far field. This effect is peculiar of ammonia sprays, which exhibit a larger temperature drop compared to, for example, Dalla Barba and Picano [10] who reported a temperature drop of less than 6 K for the acetone sprays. Such a large evaporative cooling effect generates a considerably colder environmental condition that allows a large number of droplets to sustain for all the length of the computational domain. Furthermore, the droplet patterns qualitatively follow the turbulent

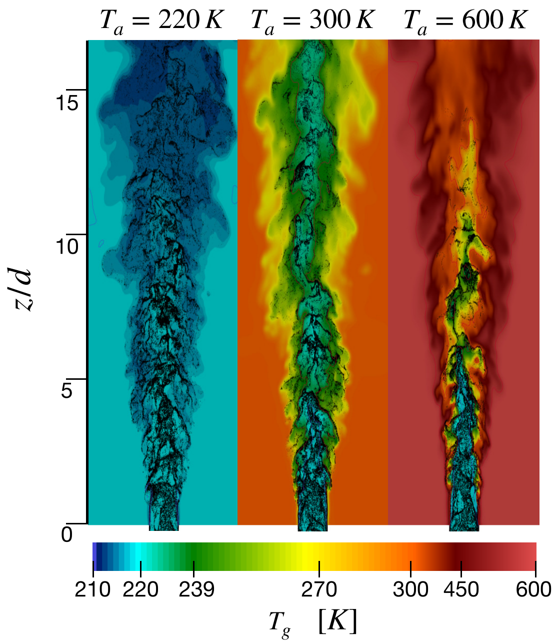

FIG. 3. Instantaneous temperature field with droplet distribution represented by black dots. From left to right: case (a) with $T_a = 220\,\mathrm{K}$, case (b) with $T_a = 300\,\mathrm{K}$, and case (c) with $T_a = 600\,\mathrm{K}$.

structures generated by the entrainment of the cold air. In the near-field region, droplets are mainly clustered along the mixing layers, while after ten diameters from the nozzle exit, droplet dispersion is more pronounced. In case (b), corresponding to $T_a = 300\,\mathrm{K}$, because of the entrainment of warmer dry air, fewer droplets survive. The strong evaporation results in a cooling of the jet region where highly clustered particles are observed along the thermal mixing layer. Some droplets are present in the hot air region, suggesting that the effect of heat conduction may be negligible and the gradient of mass concentration is still the main driving force of evaporation.

In case (c), corresponding to $T_a = 600\,\mathrm{K}$, the effect of the environmental temperature becomes more important. From a visual inspection of the $Q$-criterion field (not reported in this paper for the sake of brevity), the turbulent structures are considerably stretched due to the lower density of the gas. Droplets are clustered along the center line in the core jet region where the temperature is significantly lower than the environment. A small number of droplets, immersed in a cold gaseous ammonia cloud, is found in the hot air region, suggesting that the evaporation of dense parcels lowers the temperature of the surrounding gas to a level sufficient to survive through downstream.

Figure 4(a) displays the isosurfaces colored with the Eulerian average droplet radius. The radial and axial distances are normalized by the pipe radius and diameter, respectively. As expected, the droplet radius decreases along the downstream distance. For case (a) ($T_a = 220\,\mathrm{K}$) it is not possible to determine the liquid penetration length because the spray jet goes beyond the domain length. However, cases (b) and (c) show a reduction of the penetration length by 25% when changing the ambient temperature from 300 K–600 K. Note that the averaged isosurfaces for $\langle r_d \rangle / r_{d,0} = 1$ are nearly identical for all the cases, suggesting that the penetration of the $NH_3$-$CH_4$ mixture is comparable for different ambient temperature conditions. Further downstream, droplets in cases (b) and (c) lose 50% of the initial mass at the same height, while in case (a) the same level of loss occurs much further downstream. At this stage, in case (a) the entrainment of dry air modifies the saturation level, and in cases (b) and (c) the droplet temperature is also affected because of the convective heating. Since both of these parameters depend only on the intense turbulent mixing

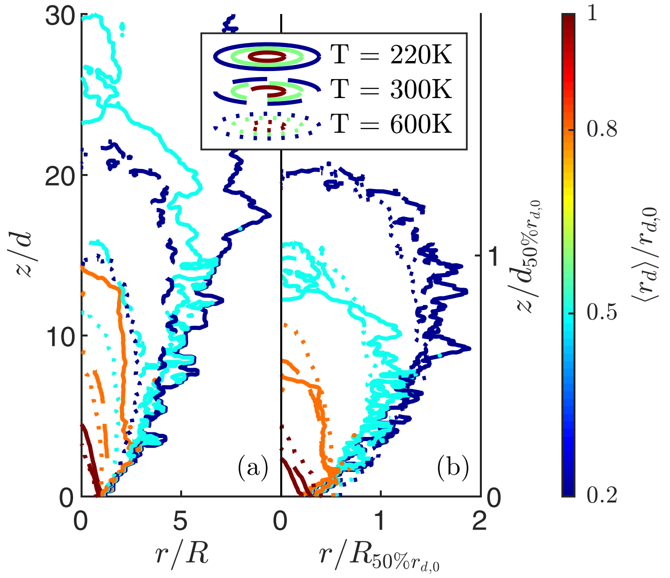

FIG. 4. Isosurfaces colored with the Eulerian averaged droplet radius. Solid line: $T_a = 220\,\mathrm{K}$; dashed line: $T_a = 300\,\mathrm{K}$; and dotted line: $T_a = 600\,\mathrm{K}$. Dark blue: $\langle r_d\rangle/r_{d,0} = 0.2$ corresponding to 1% of the initial mass; cyan: $\langle r_d\rangle/r_{d,0} = 0.5$; orange: $\langle r_d\rangle/r_{d,0} = 0.8$ corresponding to 50% of the initial mass; red: $\langle r_d\rangle/r_{d,0} = 1$ corresponding to the initial mass. In (a) the radial and axial distances are normalized by the inflow pipe radius ($R$) and diameter ($d$), respectively, whereas in (b) they are normalized by the half-radius jet width ($R_{50\%r_{d,0}}$) and length ($d_{50\%r_{d,0}}$).

due to the jet transition, which is not affected by the ambient temperature, resulting in the nearly identical isosurfaces of average radius. A more detailed investigation of the source terms is required to understand the reason behind the lack of evaporation in case (a). The trend of the droplet radius isosurfaces suggests a self-similar behavior controlled by the ambient temperature. Indeed, as shown in Fig. 4(b), normalizing the radial and axial distances by the maximum jet width and length at $\langle r_d\rangle/r_{d,0} = 0.5$, the isosurfaces for all the cases nearly collapse into one.

Figure 5 shows the Eulerian average of the droplet temperature and the carrier gas phase temperature conditioned on the presence of the droplet. Figures 5(a) and 5(b) show that, for the case at $T_a = 220\,\mathrm{K}$, $\langle T_d\rangle$ and $\langle T_{g,DC}\rangle$ (indicating the averaged gas temperature conditioned on the droplet presence) decrease along the center line confirming what was observed in Fig. 3. Note that temperature drops rapidly just outside the core jet region as well as close to the nozzle exit. This effect leads to a rapid drop of the saturation level of the mixture and possible subsequent condensation. Figure 5(c) ($T_a = 300\,\mathrm{K}$) shows the same behavior as Fig. 5(a), but the carrier phase temperature increases due to the mixing with the air [Fig. 5(d)], implying that heating effects due to the conductivity are negligible, compared to the cooling effects of the evaporation. This generates cold saturated ammonia clouds where cold droplets cluster and move downstream until they encounter regions where the entrainment of hot air is strong enough to decrease the saturation level rapidly, making the droplets vanish. Figures 5(e) and 5(f) ($T_a = 600\,\mathrm{K}$) show that the convective effects become important and the droplet temperature gains around 5–10 K. This implies that the heating due to the conduction effects are more important than the cooling effects of the evaporation and the droplet experiences a rapid evaporation. It is remarkable that the droplet temperature does not exceed the boiling condition even if they are injected in an environment at 2.3 times the saturation temperature.

Figure 6 displays the radial profiles of the average magnitude of the droplet and field velocity. The case at $T_a = 220\,\mathrm{K}$, at any stage, shows that there is little difference between $\langle U_g\rangle$ and $\langle U_d\rangle$,

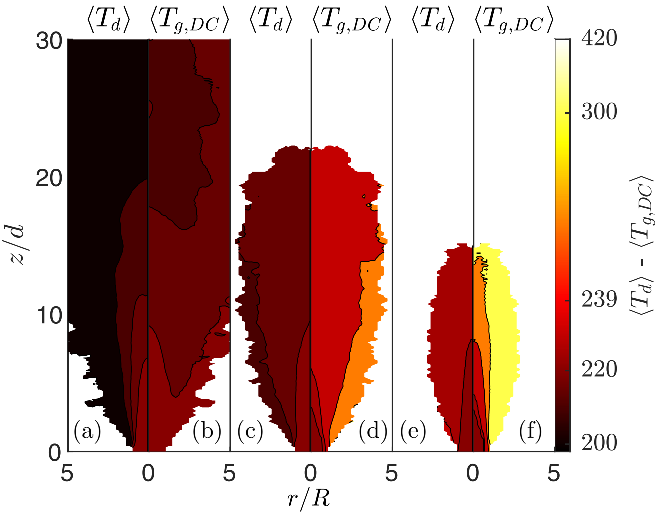

FIG. 5. Eulerian average of the droplet temperature $\langle T_d \rangle$ [(a), (c), (e)] and carrier gas phase temperature conditioned on the droplet presence $\langle T_{g,DC} \rangle$ [(b), (d), (f)]. (a) and (b): $T_a = 220\,\mathrm{K}$; (c) and (d): $T_a = 300\,\mathrm{K}$; and (e) and (f): $T_a = 600\,\mathrm{K}$.

suggesting that momentum exchange with the carrier gas is minimal. In particular, at $z/d = 2$, the carrier gas velocity is nearly identical to the droplet velocity and this behavior is not sensitive to the ambient temperature variation. Since the jet transition has not occurred yet, the temperature of the jet stream is independent of the surrounding environment, resulting in nearly the same velocity profile. Further downstream, the difference between the droplet and gas velocity becomes larger at

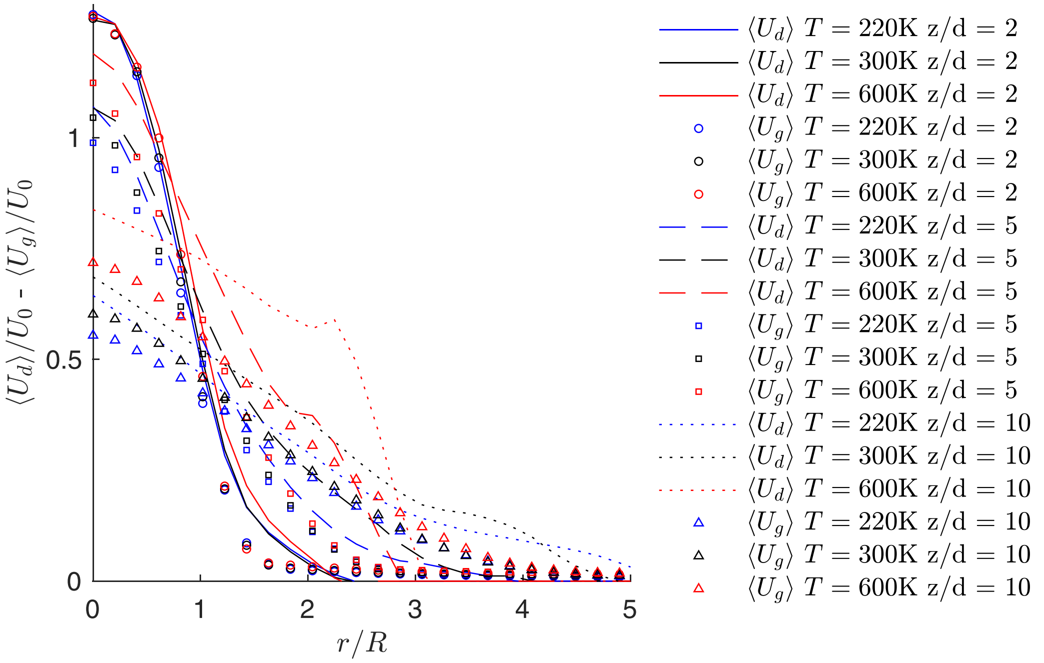

FIG. 6. Radial profiles of the magnitude of the Eulerian averaged droplet and carrier gas velocity.

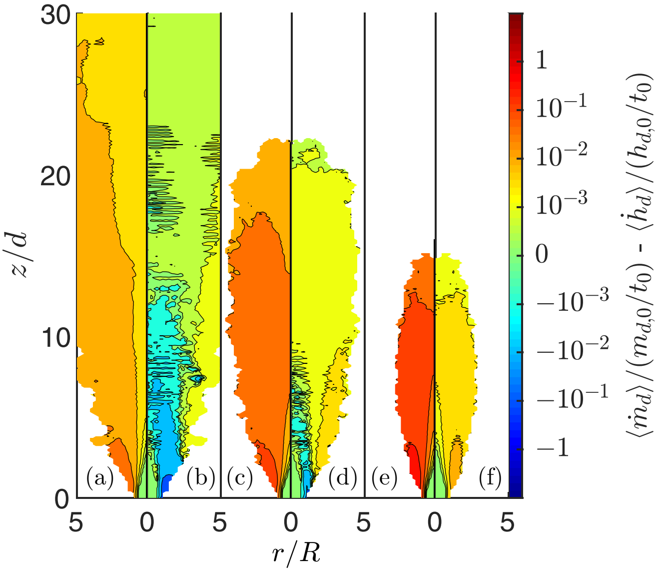

FIG. 7. Eulerian average of the normalized mass source term $\langle \dot{m}_d \rangle/(m_{d,0}/t_0)$ [(a), (c), (e)] and normalized enthalpy source term $\langle \dot{h}_d \rangle/(h_{d,0}/t_0)$ [(b), (d), (f)]. (a) and (b): $T_a = 220\,\text{K}$; (c) and (d): $T_a = 300\,\text{K}$; and (e) and (f): $T_a = 600\,\text{K}$.

higher temperature. The large exchange of the mass and momentum due to the higher environmental temperature is responsible for a rapid increase in the droplet speed, because the droplets become lighter and are easily carried by the gas flow. Indeed, with $\dot{m}_d \gg 0$ in Eq. (12), this term contributes to a strong acceleration of the droplet. Consequently, a small number of droplets escape from the low-temperature region and reach the far field. Similarly, along the mixing layer where the evaporation is enhanced by the strong mixing due to the entrainment of dry air, the droplet speed is slightly larger than the field velocity.

Figures 7(a), 7(c) and 7(e) display the Eulerian averaged mass source term and Figs. 7(b), 7(d) and 7(f) show the enthalpy source term at the ambient temperature of 220, 300, and 600 K, respectively. The mass source term is normalized by the reference value $m_{d,0}/t_0$, where $m_{d,0} = (4/3)\,\pi\, r_{d,0}^3\, \rho_l$ and $t_0 = d/U_0$, while the enthalpy is normalized by $h_{d,0}/t_0$ with $h_{d,0} = m_{d,0}\, C_{p,l}\, T_{d,0}$. In Fig. 7(a), the mixing layer in the near field is the only region where droplets experience a considerable level of evaporation $[\langle \dot{m}_d \rangle/(m_{d,0}/t_0) \approx 10^{-1.5}]$. The center line is characterized by an expanding region of mild evaporation $[\langle \dot{m}_d \rangle/(m_{d,0}/t_0) \approx 10^{-2.5}]$ due to the intense cooling of the carrier phase combined with the large latent heat, resulting in a penetration length significantly longer than the case with the warmer environment. Figure 7(b) shows three different behaviors of the enthalpy source term: (i) the core jet region for $z/d \leqslant 15$ where the $\langle \dot{m}_d \rangle/(m_{d,0}/t_0) < 0$, suggesting that the evaporative cooling effects are stronger than the convective heating, (ii) the mixing layer where $\langle \dot{m}_d \rangle/(m_{d,0}/t_0) > 0$, because of the entrainment of warmer dry air, and (iii) the far field where thermal equilibrium is dominant. Figure 7(c) shows a more intense evaporation in the mixing layer where $\langle \dot{m}_d \rangle/(m_{d,0}/t_0) \approx 10^{-1.5}$. This effect is due to the entrainment of hotter dry air from the environment compared to the previous case. The enthalpy source term [Fig. 7(d)] is slightly positive everywhere ($\approx 10^{-3}$), being close to the thermal equilibrium due to a larger enthalpy exchange in the mixing layer near field, where this difference is attributed to the hotter entrained air. A region of negative enthalpy source term is found when the droplets start evaporating, suggesting that droplets cool down even if the surrounding is warmer.

The case at $T_a = 600\,\text{K}$, [Fig. 7(e)] shows a stronger evaporation in the mixing layer with $\langle \dot{m}_d \rangle/(m_{d,0}/t_0) \approx 0.5$. In this region, Figs. 5(e) and 5(f) show that the droplets warm up because

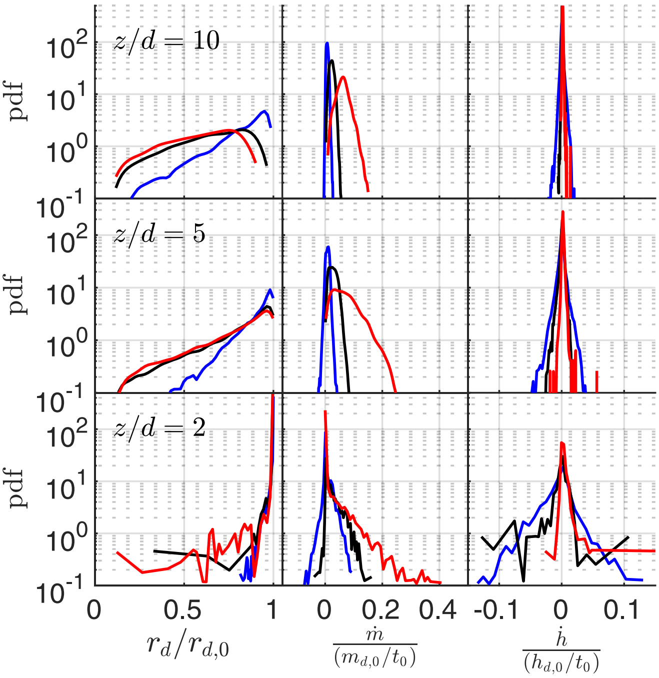

FIG. 8. Probability density functions of droplet radius, mass, and enthalpy source terms at $z/d \approx 2$, 5, and 10. Blue line: $T_a = 220\,\mathrm{K}$; black line: $T_a = 300\,\mathrm{K}$; and red line: $T_a = 600\,\mathrm{K}$.

of the environment and this substantially enhances the evaporation. Furthermore, because of the entrainment, the mass exchange remains higher. Compared to the case at $T_a = 300\,\mathrm{K}$, where $\langle \dot{m}_d \rangle/(m_{d,0}/t_0) \approx 10^{-2.5}$ becomes nearly zero close to the end of the jet, the case at $T_a = 600\,\mathrm{K}$ shows a noticeable level of mass source term, then droplets vanish extremely fast. The enthalpy exchange term [Fig. 7(f)] is largely positive everywhere [$\langle \dot{h}_d \rangle/(h_{d,0}/t_0) > 10^{-2}$], except in the core jet region of the near field. The entrainment of hot air enhances an intense heat exchange behavior. Recalling from Fig. 5 that the temperature of the droplet slightly increases, it is concluded that the effect of the convective fluxes is prevalent on evaporation cooling.

The reason behind the longer region at $\langle \dot{m}_d \rangle/(m_{d,0}/t_0) \approx 0$ is now discussed through the probability density function (pdf) of the droplet radius, mass and enthalpy source terms at $z/d = 2$, 5, and 10 (Fig. 8). At $z/d = 2$ the pdf of droplet radius is mainly concentrated at $r_d/r_{d,0} \approx 1$, with a low probability of finding $r_d/r_{d,0} \leqslant 0.5$ for the higher temperature. Further downstream, the range of the pdf for the case at $T_a = 220\,\mathrm{K}$ increases as expected, while for the other cases it remains almost constant. Note that the distribution is not affected by the ambient temperature for the cases at $T_a = 300\,\mathrm{K}$ and 600 K, suggesting that the evaporation time scale is not affected by the ambient temperature in this range.

The mass source terms shows different behavior between the cases at $T_a = 220\,\mathrm{K}$ and $T_a \geqslant 300\,\mathrm{K}$. At any stage, for $T_a = 220\,\mathrm{K}$ the pdf shows a non-zero probability of finding $\dot{m}_d/(m_{d,0}/t_0) < 0$, with the pdf centered at $\dot{m}_d/(m_{d,0}/t_0)$ slightly greater than zero, confirming that the average $\langle \dot{m}_d \rangle/(m_{d,0}/t_0) \approx 0$. The condensation of droplets is a consequence of the Spalding model; although the saturated molar fraction $X_{\mathrm{sat}}$ remains almost constant since the saturated vapor pressure is a function of the droplet temperature only [$X_{\mathrm{sat}} = p_{\mathrm{sat}}(\langle T_d \rangle)/p_a$], the corresponding saturated mass fraction ($Y_{\mathrm{sat}} = X_{\mathrm{sat}} W_{NH_3}/[X_{\mathrm{sat}} W_{NH_3} + (1 - X_{\mathrm{sat}}) W_{\mathrm{mix}}]$) is a function of the surrounding mixture through the term $W_{\mathrm{mix}} = X_{O_2} W_{O_2} + X_{N_2} W_{N_2} + X_{CH_4} W_{CH_4}$, varying in the range $0.016 \leqslant W_{\mathrm{mix}} \leqslant 0.029$ kg/mol. In addition, $r_d/r_{d,0} \leqslant 1$ suggests that the condensing time scale is much larger than flow time scale

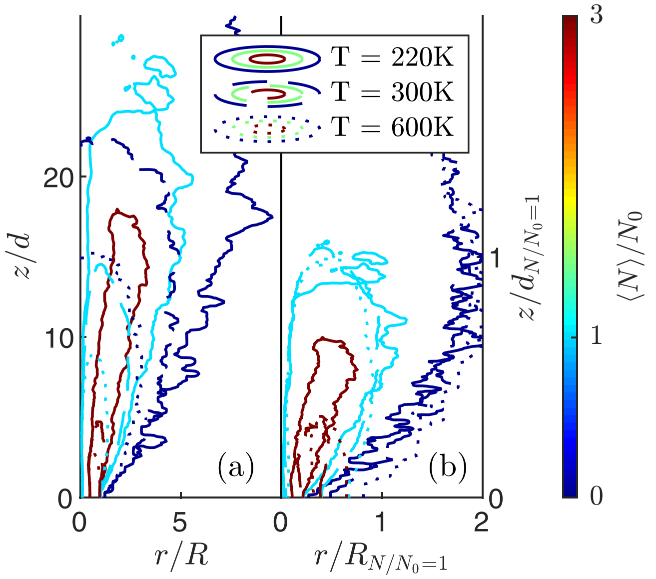

FIG. 9. Isosurfaces of Eulerian average droplet distribution. Solid line: $T_a = 220\,\mathrm{K}$; dashed line: $T_a = 300\,\mathrm{K}$; and dotted line: $T_a = 600\,\mathrm{K}$. Dark blue: $\langle N\rangle/N_0 = 0$, light blue: $\langle N\rangle/N_0 = 1$, red: $\langle N\rangle/N_0 = 3$. In (a) the radial and axial distances are normalized by the inflow pipe radius ($R$) and diameter ($d$), respectively, whereas in (b) they are normalized by $\langle N\rangle/N_0 = 1$ jet width ($R_{\langle N\rangle/N_0=1}$) and length ($d_{\langle N\rangle/N_0=1}$).

and droplets have already evaporated before condensing. Furthermore, the enthalpy source term is slightly negative only at $z/d = 2$, implying that the heating due to condensation is negligible compared to convective cooling. At higher ambient temperatures, we have always $\langle \dot{m}_d\rangle/(m_{d,0}/t_0) \geqslant 0$, suggesting that the change of mixture effect is balanced by the growth of the droplet temperature. Concerning the enthalpy source term in Fig. 8, the pdf is centered at zero for all the stages because the thermal equilibrium is achieved everywhere.

Figure 9(a) displays the averaged distribution of the number of droplets normalized by that at the exit of the nozzle. Note that the number of droplets is maximized ($\langle N\rangle/N_0 \leqslant 3$) in the mixing layer region. This effect is referred to as the turbophoresis by the pipe wall, leading to clustering the majority of the droplets near the wall. Nonetheless, $\langle N\rangle/N_0 \sim 1$ for about 60% of the penetration length and 50% of the width of the droplets spatial distribution. This underlines the presence of self-similarity in the average droplet distribution due to the environmental temperature, as highlighted in Fig. 9(b). Indeed, the isosurface at $\langle N\rangle/N_0 = 3$ representing the turbophoresis effect does not follow the self-similarity scaling, but is expected to be independent of the environmental temperature.

Finally, the droplet dispersion characteristics are examined via a three-dimensional (3D) Voronoi tessellation. The Voronoi algorithm has been applied to evaluate the droplet preferential segregation [14] in 2D diagrams. In this study, the methodology proposed by [14] is extended to a three-dimensional analysis as done in other fields [34]. As a brief summary, each droplet is assigned an index $V$ representing the distance from the closest droplets: small and large $V$ indicates a dense and sparse region of droplets, respectively. Previous studies attempted quantification of the clustering behavior of particles [35], and Battista *et al.* [36] defined a clustering index based on the number of droplets inside an arbitrary control volumes as a measure of droplet density. In this paper, we removed the arbitrariness employing the Voronoi volumes as a measure of the local droplet density. The clustering index is herein defined as $K = \langle V''^2\rangle^{0.5}/\langle V\rangle$, where $\langle V\rangle$ is the Eulerian average and $\langle V''^2\rangle^{0.5}$ is the standard deviation of the Voronoi index $V$. If the droplets were purely randomly distributed in the field, the droplet distribution would be driven by the Poisson process, for which

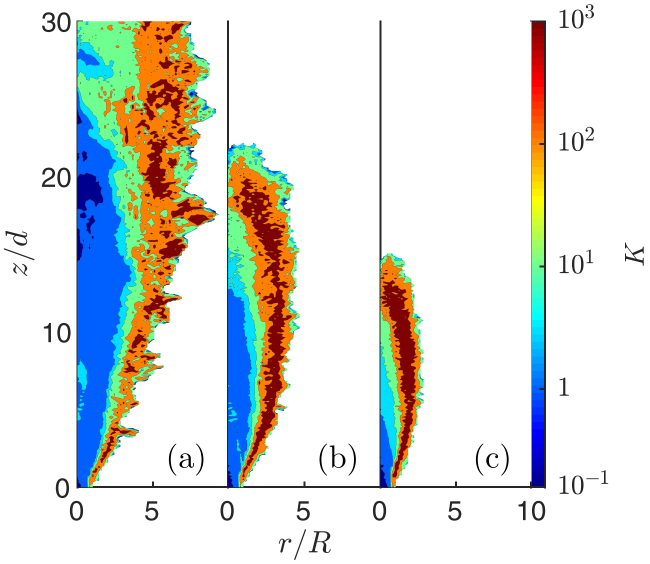

FIG. 10. Eulerian average of the droplet clustering index $K$. (a) $T_a = 220\,\mathrm{K}$, (b) $T_a = 300\,\mathrm{K}$, and (c) $T_a = 600\,\mathrm{K}$.

the mean and standard deviation of the inter-droplet distance would coincide ($K = 1$). If $0 \leqslant K < 1$, the interdroplet distances are similar and tend to remain invariant, implying that the droplets are dispersed. When $K > 1$, the interdroplet distance varies, implying that the droplets preferentially segregate in clusters. The larger $K$, the stronger the effect of the preferential segregation is.

Figure 10 shows the Eulerian field of the clustering index. For any environmental temperature, $K$ is slightly negative near the nozzle exit ($z/d < 2$) along the center line and $K \gg 1$ for $r/R \approx 1$, confirming that the droplets are highly dispersed in the core of the pipe, and subsequently clustered for the turbophoresis close to the pipe wall. At $T_a = 220\,\mathrm{K}$ [Fig. 10(a)] and, less so in $T_a = 300\,\mathrm{K}$ [Fig. 10(b)], $K > 1$ in the jet transition region. Such a mild clustering is due to the effect of the Stokes drag, which is important during the turbulent transition. In fact, the Stokes number based on the Kolmogorov scale, $St_\eta \approx 2$ in this region (not shown for brevity). The effect of the Stokes drag is to segregate the droplets inside the small scale vortices generated by the turbulent transition.

On the other hand, for the case at $T_a = 220\,\mathrm{K}$ [Fig. 10(a)], a highly dispersed region is found in the far field. In this region, as the turbulent jet is fully developed and the temperature is considerably low due to the evaporation, the turbulent structures are relatively large and slow. As the droplets are largely evaporated ($0.5 \leqslant \langle r_d \rangle / r_{d,0} \geqslant 0.8$) (see Fig. 4) and have a small inertia, corresponding to a mass less than the 50% of the initial one), they follow these large structures, increasing the interdroplet distance and slowing down its temporal variation. At higher environmental temperature (Fig. 10), the entrainment of hot air prevents the generation of a low-temperature dispersed region.

In all cases, a region with $K \gg 1$ is observed along the mixing layer. Figure 10(a) shows that $K$ ranges between $10^2$ and $10^3$, while for the hotter cases [Figs. 10(b) and 10(c)] $K$ is much larger, even above $10^3$. The large variation in all cases is attributed to the moving interface between the jet stream, largely populated by droplets, and the outer region where they are absent. Moreover, at higher environment temperature, the increasing difference between the velocity of the field and the droplet speed (Fig. 6) induces a drag, which may further segregate the droplets in clusters along the mixing layer. The large latent heat cools down the surroundings of the cluster, slowing down the evaporation enhanced by the entrainment of the hot air. This effect is significant at $T_a = 600\,\mathrm{K}$ [Fig. 10(c)] where $K \gg 1$ is found immediately after the jet transition ($z/d \leqslant 7$).

## V. CONCLUSIONS

Three cases of direct numerical simulations of liquid ammonia spray jet with different ambient temperature were performed and the effects of the hot air entrainment on the spray dynamics were extensively investigated, highlighting the unique characteristics of the ammonia droplet dynamics due to the large latent heat. The main findings are summarized in the following.

First, the low-temperature case shows a strong cooling effect of the spray, resulting in a long penetration length, while increasing the surrounding temperature drastically reduces the penetration length. Second, for all the conditions considered, droplets never experienced boiling, implying that the cooling caused by the large latent heat is dominant over the heat conduction of the droplets even in a significantly hot environment where the temperature is several times higher than the boiling temperature. Third, at low surrounding temperature conditions, ammonia droplets experience condensation due to the effect of the $NH_3$-$CH_4$-air mixing. This effect allows the droplets to survive along the center line for a longer distance compared to the warmer environments. Fourth, increasing the environmental temperature brings a higher level of preferential segregation along the mixing layer. These clusters can survive longer downstream thanks to the cold evaporated cloud resulting from the large latent heat of evaporation. Finally, a self-similarity was identified for the droplet radius and distribution isosurfaces where the effects of the condensation and turbophoresis are not pronounced.

## ACKNOWLEDGMENTS

The authors acknowledge the support of the Italian Ministry of University and Research (MIUR) and King Abdullah University of Science and Technology (KAUST). Computational resources were provided by the KAUST Supercomputing Laboratory (KSL).

---

[1] F. van der Ploeg and A. Rezai, Stranded assets in the transition to a carbon-free economy, Annu. Rev. Resour. Econ. **12**, 281 (2020).

[2] M. Xu, Y. Zhang, W. Zeng, G. Zhang, and M. Zhang, Flash boiling: Easy and better way to generate ideal sprays than the high injection pressure, SAE Int. J. Fuels Lubr. **6**, 137 (2013).

[3] E. C. Okafor, K. K. A. Somarathne, A. Hayakawa, T. Kudo, O. Kurata, N. Iki, and H. Kobayashi, Towards the development of an efficient low-nox ammonia combustor for a micro gas turbine, Proc. Combust. Inst. **37**, 4597 (2019).

[4] O. Kurata, N. Iki, T. Matsunuma, T. Inoue, T. Tsujimura, H. Furutani, H. Kobayashi, and A. Hayakawa, Performances and emission characteristics of $NH_3$–air and $NH_3$–$CH_4$–air combustion gas-turbine power generations, Proc. Combust. Inst. **36**, 3351 (2017).

[5] H. Kobayashi, A. Hayakawa, K. K. A. Somarathne, and E. C. Okafor, Science and technology of ammonia combustion, Proc. Combust. Inst. **37**, 109 (2019).

[6] A. Valera-Medina, H. Xiao, M. Owen-Jones, W. I. David, and P. Bowen, Ammonia for power, Prog. Energy Combust. Sci. **69**, 63 (2018).

[7] F. Verkamp, M. Hardin, and J. Williams, Ammonia combustion properties and performance in gas-turbine burners, in *Symposium (International) on Combustion*, Vol. 11 ( Elsevier, Amsterdam, 1967), pp. 985–992.

[8] E. C. Okafor, H. Yamashita, A. Hayakawa, K. K. A. Somarathne, T. Kudo, T. Tsujimura, M. Uchida, S. Ito, and H. Kobayashi, Flame stability and emissions characteristics of liquid ammonia spray co-fired with methane in a single stage swirl combustor, Fuel **287**, 119433 (2021).

[9] N. Scapin, F. Dalla Barba, G. Lupo, M. E. Rosti, C. Duwig, and L. Brandt, Finite-size evaporating droplets in weakly compressible homogeneous shear turbulence, J. Fluid Mech. **934**, A15 (2022).

[10] F. Dalla Barba and F. Picano, Clustering and entrainment effects on the evaporation of dilute droplets in a turbulent jet, Phys. Rev. Fluids **3**, 034304 (2018).

[11] J. Wang, F. Dalla Barba, and F. Picano, Direct numerical simulation of an evaporating turbulent diluted jet-spray at moderate Reynolds number, Int. J. Multiphase Flow **137**, 103567 (2021).

[12] P. Ciottoli, F. Battista, R. M. Galassi, F. Dalla Barba, and F. Picano, Direct numerical simulations of the evaporation of dilute sprays in turbulent swirling jets, Flow, Turbul. Combust. **106**, 993 (2021).

[13] Y.-C. Chen, S. H. Stårner, and A. R. Masri, A detailed experimental investigation of well-defined, turbulent evaporating spray jets of acetone, Int. J. Multiphase Flow **32**, 389 (2006).

[14] Manish M and S. Sahu, Analysis of droplet clustering in air-assist sprays using voronoi tessellations, Phys. Fluids **30**, 123305 (2018).

[15] P. Jenny, D. Roekaerts, and N. Beishuizen, Modeling of turbulent dilute spray combustion, Prog. Energy Combust. Sci. **38**, 846 (2012).

[16] W. A. Sirignano, Fuel droplet vaporization and spray combustion theory, Prog. Energy Combust. Sci. **9**, 291 (1983).

[17] W. A. Sirignano, *Fluid Dynamics and Transport of Droplets and Sprays* (Cambridge University Press, Cambridge, 2010).

[18] B. Abramzon and W. Sirignano, Droplet vaporization model for spray combustion calculations, Int. J. Heat Mass Transf. **32**, 1605 (1989).

[19] R. Miller, K. Harstad, and J. Bellan, Evaluation of equilibrium and non-equilibrium evaporation models for many-droplet gas-liquid flow simulations, Int. J. Multiphase Flow **24**, 1025 (1998).

[20] D. B. Spalding, Combustion of liquid fuels, Nature (London) **165**, 160 (1950).

[21] G. Godsave, Studies of the combustion of drops in a fuel spray-the burning of single drops of fuel, in *Symposium (International) on Combustion*, Vol. 4 ( Elsevier, Amsterdam, 1953), pp. 818–830.

[22] M. Yuen and L. Chen, On drag of evaporating liquid droplets, Comb. Sci. Tech. **14**, 147 (1976).

[23] L. Angelilli, P. P. Ciottoli, F. Picano, M. Valorani, and H. G. Im, Assessment of subgrid dispersion models for large-eddy simulations of turbulent jet flows with dilute spray droplets, Phys. Fluids **34**, 073305 (2022).

[24] See Supplemental Material at http://link.aps.org/supplemental/10.1103/PhysRevFluids.7.114301 for grid convergence assessment.

[25] S. Elghobashi and G. Truesdell, On the two-way interaction between homogeneous turbulence and dispersed solid particles. I: Turbulence modification, Phys. Fluids **5**, 1790 (1993).

[26] G. Truesdell and S. Elghobashi, On the two-way interaction between homogeneous turbulence and dispersed solid particles. II. particle dispersion, Phys. Fluids **6**, 1405 (1994).

[27] A. Wierzba, Deformation and breakup of liquid drops in a gas stream at nearly critical weber numbers, Exp. Fluids **9**, 59 (1990).

[28] J. G. Eggels, F. Unger, M. Weiss, J. Westerweel, R. J. Adrian, R. Friedrich, and F. T. Nieuwstadt, Fully developed turbulent pipe flow: A comparison between direct numerical simulation and experiment, J. Fluid Mech. **268**, 175 (1994).

[29] G. Xu and R. Antonia, Effect of different initial conditions on a turbulent round free jet, Exp. Fluids **33**, 677 (2002).

[30] T. C. Lau and G. J. Nathan, The effect of stokes number on particle velocity and concentration distributions in a well-characterised, turbulent, co-flowing two-phase jet, J. Fluid Mech. **809**, 72 (2016).

[31] J. Kuerten, Subgrid modeling in particle-laden channel flow, Phys. Fluids **18**, 025108 (2006).

[32] J. Qian and C. K. Law, Regimes of coalescence and separation in droplet collision, J. Fluid Mech. **331**, 59 (1997).

[33] H. G. Weller, G. Tabor, H. Jasak, and C. Fureby, A tensorial approach to computational continuum mechanics using object-oriented techniques, Comput. Phys. **12**, 620 (1998).

[34] L. Andronov, J. Michalon, K. Ouararhni, I. Orlov, A. Hamiche, J.-L. Vonesch, and B. P. Klaholz, 3dclustervisu: 3d clustering analysis of super-resolution microscopy data by 3d voronoi tessellations, Bioinformatics **34**, 3004 (2018).

[35] R. Shaw, A. Kostinski, and M. L. Larsen, Towards quantifying droplet clustering in clouds, Q. J. R. Meteorol. Soc. **128**, 1043 (2002).

[36] F. Battista, F. Picano, G. Troiani, and C. M. Casciola, Intermittent features of inertial particle distributions in turbulent premixed flames, Phys. Fluids **23**, 123304 (2011).